Honda Research Institute EU
Honda Research Institute Europe GmbH
https://www.honda-ri.de/

A Study of a modern transonic low-aspect ratio fan rotor in a small turbofan engine

Toyotaka Sonoda, Rainer Schnell, Toshiyuki Arima, Giles Endicott, Eberhard Nicke

2013

Preprint:

This is an accepted article published in ASME Turbo Expo 2013. The final authenticated version is available online at: https://doi.org/[DOI not available]

Proceedings of ASME Turbo Expo 2013
GT2013
June 3-7, 2013, San Antonio, Texas, USA

GT2013-95447

A STUDY OF A MODERN TRANSONIC FAN ROTOR IN A LOW REYNOLDS NUMBER REGIME FOR A SMALL TURBOFAN ENGINE

Toyotaka Sonoda
Honda R&D Co. Ltd.
Aircraft Engine R&D Center
Saitama 351-0193, Japan

Rainer Schnell
German Aerospace Center (DLR)
Institute of Propulsion Technology
D-51147 Cologne, Germany

Toshiyuki Arima
Honda R&D Co. Ltd.
Fundamental Technology
Research Center
Saitama 351-0193, Japan

Giles Endicott
Honda Research Institute
Europe GmbH
D-63073 Offenbach/Main,
Germany

Eberhard Nicke
German Aerospace Center (DLR)
Institute of Propulsion Technology
D-51147 Cologne, Germany

ABSTRACT

In this paper, Reynolds effects on a modern transonic low-aspect-ratio fan rotor (Baseline) and the re-designed (optimized) rotor performance are presented with application to a small turbofan engine. The re-design has been done using an in-house numerical optimization system in Honda and the confirmation of the performance was carried out using DLR's TRACE RANS stage code, assessed with respect to experimental data obtained from a small scale compressor rig in Honda. The baseline rotor performance is evaluated at two Reynolds number conditions, a high Reynolds condition (corresponding to a full engine scale size) and a low Reynolds number condition (corresponding to the small scale compressor rig size), using standard ISA conditions. The performance of the optimized rotor was evaluated at the low Reynolds number condition. The CFD results show significant discrepancies in the rotor efficiency (about 1% at cruise) between these two points due to the different Reynolds numbers. The optimized rotor's efficiency is increased compared to the baseline. A unique negative curvature region close to the leading edge on the pressure surface of the optimized rotor is one of the reasons why the optimized rotor is superior to the baseline.

NOMENCLATURE

c	blade actual chord
Cp	specific heat at constant pressure
M	Mach number
p	static pressure
Po	total pressure
R	gas constant
Re	Reynolds number based on blade actual chord
r	distance in radial direction
To	total temperature
U	blade speed
v	flow velocity
X	distance in axial direction
γ	ratio of specific heat capacities Cp/Cv
ρ	density

Subscripts

1	inlet station of upstream of rotor leading edge
2	outlet station of rotor / inlet station of OGV
3	outlet station of downstream of OGV
tip	blade tip
θ	angle in circumferential direction

Abbreviations

CFD	computational fluid dynamics
CRS	cruise condition
EXP	experiment
MCM	max-climb condition
OGV	outlet guide vane
PE	peak efficiency point
TCL	tip clearance
T/O	take-off condition

Copyright © 2013 by ASME

INTRODUCTION

There are many publications on the effect of Reynolds number on axial flow compressor. For example, first works on the subject demonstrated the correlation between performance and Reynolds numbers [1]. More recently, as a result of the remarkable development of computer technology, aerodynamic optimization methods composed of both CFD and numerical optimization algorithms have been applied to both two dimensional [2-4] and/or three dimensional compressor outlet guide vane design studies [5-6] in order to provide better performance and/or to find new design concepts in the low Reynolds number regime. On the other hand, there are few papers on the effect of Reynolds number on three dimensional compressor rotor blades, especially for transonic fan rotors in turbofan engines. This is because the rotors that have been investigated are predominantly used for medium or large sized turbofan engines, and therefore there have been no significant issues due to Reynolds effects. However, when applied to smaller sized turbofan engines, the rotor performance appears to be affected by Reynolds effects and therefore it is worth investigating the Reynolds effects when looking for more compact and efficient transonic rotor design solutions.

The main objectives in this paper are 1) to clarify the extent of Reynolds effects on the baseline rotor's performance, 2) to confirm the efficiency improvement of the redesigned (optimized) rotor using DLR-TRACE solver [7-10], and finally 3) to investigate the reasons why the optimized rotor has superior performance.

The remainder of this paper is layed out as follows; experimental and numerical methods for the assessment of DLR TRACE solver are described first. Subsequently, the assessment results of TRACE, effect of Reynolds number on rotor performance for baseline rotor are discussed, and finally the re-designed rotor performance is estimated by DLR code and finally the reason why the optimized rotor is superior to the baseline is discussed.

Optimization and Optimized Rotor Performance by Honda

Recently Honda has improved the efficiency of its fan rotor using an in-house numerical optimization system [11]. The optimization of the rotor was performed using the CFD simulations described in [12] in order to find a geometric design superior to the baseline.

The manipulation of the blade geometry enabling the shape optimization was performed using "free form deformation" (FFD) of the computational mesh. Pioneered by Sederberg and Parry [13] in 1986, the method provides a user intuitive form of shape modification, analogous to the compression and expansion of the design formed in rubber. The movement of the control grid results in the smooth deformation of the sphere it contains. Using this method the geometry, defined as a set of co-ordinates in space is embedded within a parametric volume defined by the Euclidean position of a set of control points. This is demonstrated in Fig. 1, showing the deformation of a sphere using FFD.

The FFD grid we used for the rotor passage as shown in Fig.2 comprised of 6 control points in the axial direction, 4 points in the circumferential direction and 7 points in the radial direction which formed a control volume encompassing all node points of the rotor blade. The spheres linked by lines represent the FFD control volume which allows the manipulation of the flow domain, resulting in changes to the blade surface. The upper surface seen is the hub while the visible side is the pressure surface periodic boundary of the CFD grid. The upstream boundary is on the left of the image, while the outlet is on the right hand side. The control points at the axial extents remained fixed, together with the circumferentially outside control points. The other 56 were moved circumferentially, resulting in 56 design variables for optimization. Limits were placed on the deformation to ensure a low number of failures of the mesh as a result of its manipulation by the FFD.

A generational, stochastic search method, Particle swarm optimization [14] was used for the optimization process due to its good performance in benchmarks. The objective function was based upon three flight conditions, take-off, cruise, and max-climb at each peak efficiency point (PE), respectively. The main point of the flight envelope, cruise (CRS) was our main objective and optimized directly, while the take–off (T/O) and max climb (MCM) conditions were constrained using ramped penalty functions to be equal to or better than the baseline. For all three conditions the simulation was run close to the peak efficiency point. In all 300 generations were used, bringing the objective function down considerably, and maintaining the constraints set.

Figure 3 shows the comparison of the baseline with the re-designed optimized rotor at the three speed-lines, T/O, CRS, and MCM. The optimized rotor efficiency at PE, CRS is 0.88% higher than the baseline rotor. In order to confirm the numerically achieved efficiency level, Honda asked DLR-Cologne to evaluate the stage performance using the TRACE CFD solver.

It should be noted that in the optimization a rotor that has a robustness of the tip clearance variation has been sought. Therefore about three times of the tip clearance of a small scale high-speed single stage compressor rig shown in the next chapter has been used.

Copyright © 2013 by ASME

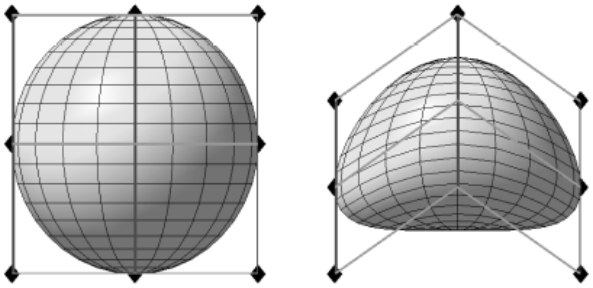


Figure 1. A depiction of Free Form Deformation.

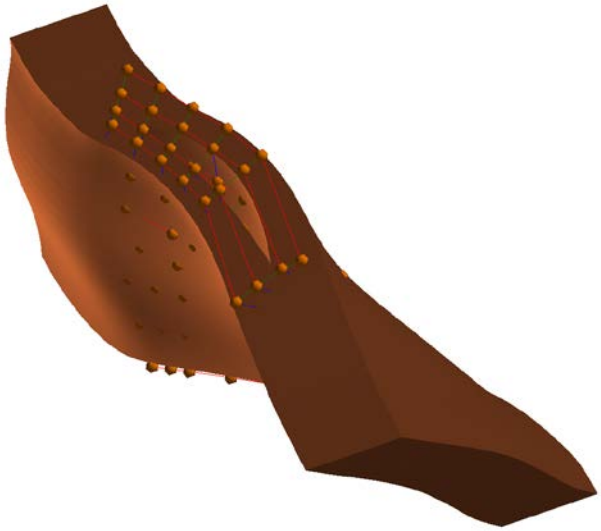


Figure 2. Blade centred computational domain, showing the rotor blade as a hole, obtained from [11].

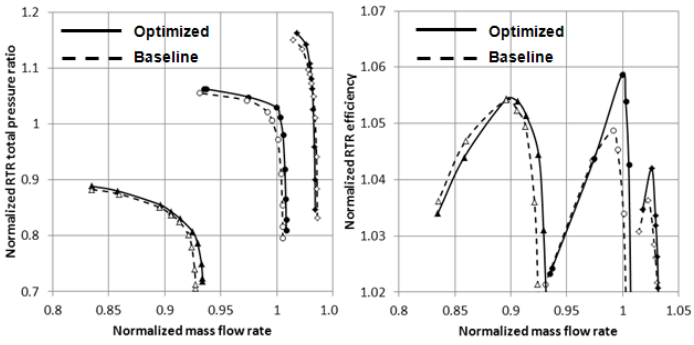


Figure 3. Comparison of rotor performance for baseline and optimized rotors; left: total pressure ratio, right: efficiency, obtained from [11].

APPROACH METHODS

Experimental Method

Experiments were carried out in a small scale high-speed single stage research compressor at the Honda Aircraft Engine R&D Center (see Fig. 4). The small scale rig was used in lieu of the full scale one as it has a ground level atmospheric inlet condition which directly corresponds to the design cruise (low Reynolds number) condition and thus is convenient as it reduces both development time and costs.

At the design speed (CRS), in the case of full scale engine, the Reynolds numbers based on rotor tip chord and hub chord are $3.5x10^6$ and $1.3x10^6$, respectively. For the small scale rig, they are $1.3x10^6$ (tip) and $4.6x10^5$ (hub), respectively. Therefore there may be a possibility of deterioration of performance close to the hub, because the order of Reynolds number is 10^5 and the relative Mach number at the hub inlet is relatively high (about 0.7) and the camber angle is the maximum. The rotor tip clearance used was 0.1mm and 0.13mm at CRS and T/O conditions, respectively. These values were estimated using NASTRAN based FEM analysis. The direct measurement of the tip clearance, however, has not been done.

In the experimental rig, ambient air is led through a bell-mouth and a settling chamber with flow conditioning screens and a contraction before entering the compressor stage. The rotor is driven by a 300KW DC-drive with the shaft speed and power measured using a torque-meter. The mass flow rate is measured at the bell-mouth while the inlet total pressure and temperature are measured by probes located inside the settling chamber. The stage exit total pressure and temperature are measured by tandem probes located downstream of the OGV. Two tandem probes for total pressure measurement and two tandem probes for total temperature measurement are circumferentially distributed and traversed in the circumferential direction by a traversing ring concurrently in order to estimate the circumferential variation of the experiments. The OGV exit flow angle is obtained from a single five-hole probe installed to the traverse ring where the probe is circumferentially traversed at each span-wise position.

As the compressor performance map characteristics are significantly changed when the probes are inserted to a passage downstream of the rotor (upstream of the OGV), only static pressure was measured at the casing wall between the rotor-trailing edge and OGV-leading edge. Since the flow-field is not measured between the rotor and the OGV, the rotor exit flow field needs to be predicted using the measured data together with some assumptions. That is, the rotor exit total pressure was assumed to be equal to the maximum value of OGV wake. The rotor exit total temperature was assumed to be equal to the mass averaged value of OGV wake. These assumptions have also been used by Wennerstrom's high-through flow transonic axial compressor stage [15]. It should be noted that the assumption on the pressure was supported by CFD data of the circumferential wake pattern.

Copyright © 2013 by ASME

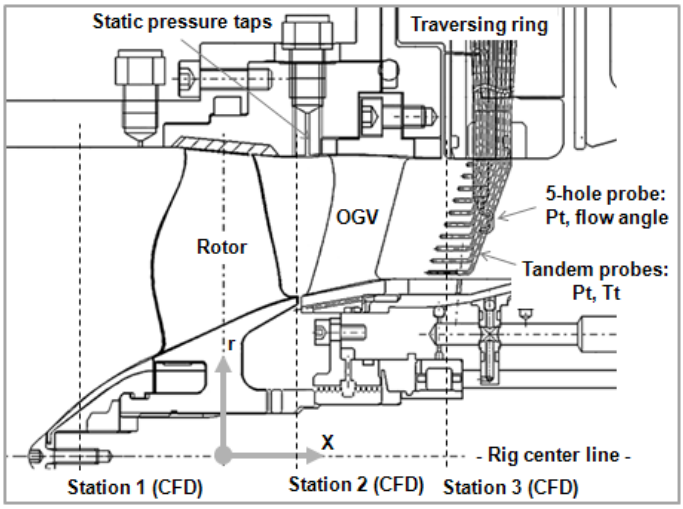


Figure 4. Small scale high-speed single stage research fan compressor rig.

The rotor exit flow angle was calculated by applying the Euler turbine equation to the rotor and the simple radial equilibrium equation to the rotor exit using an iterative procedure, see below.

Set $To_2(r) = To_3(r)$, $Po_2(r) = Po_3(r)$.

(1) Calculate $v_{2\theta}(r)$ profile using
$Cp\left(To_2(r) - To_1(r)\right) = U\left(v_{2\theta}(r) - v_{1\theta}(r)\right)$.

(2) Assume pressure profile $p_2(r)$.

(3) Compute Mach number profile $M_2(r)$ using

$$M_2(r) = \sqrt{\frac{2}{\gamma - 1}\left\{1 - \left(\frac{p_2(r)}{Po_2(r)}\right)^{\frac{\gamma-1}{\gamma}}\right\}}$$

(4) Compute density profile $\rho_2(r)$ using

$$\rho_2(r) = \left(\frac{Po_2(r)}{R \cdot To_2(r)}\right) \Bigg/ \left(1 + \frac{\gamma - 1}{2} M_2(r)^2\right)^{\frac{1}{\gamma-1}}$$

(5) Update pressure profile $p_2(r)$ using

$$p_2(r) = p(r_{tip}) - \int_r^{r_{tip}} \rho_2(r) \frac{v_{2\theta}(r)^2}{r} dr$$

(6) If pressure profile is not converged then repeat steps (4)-(6).

The measurement accuracy of rotor efficiency based on the torque meter is ± 0.15%.

Numerical Method

For the numerical simulations for the confirmation of the rotor design improvement, the flow solver TRACE [7-10] was used. The code is a cell-centered finite volume, Reynolds-averaged Navier-Stokes solver that has been developed at the Institute of Propulsion Technology at DLR, in particular in the context of turbomachinery specific applications. Its applicability and validation to a wide range of turbomachinery specific configurations comprising aerodynamic as well as acoustic analysis mainly comprising tonal fan noise has been demonstrated in previous studies [7-10]. For turbulence closure, a one-equation Spalart-Allmaras as well as a two-equation k-omega turbulence model are available, both equipped with corresponding extensions for turbomachinery applications. For all present investigations the two-equation model was employed. The state variables are extrapolated to the cell faces with a standard MUSCL (Monotone Upstream-centered Scheme for Conservation Laws) approach of second or third order accuracy respectively. The convective fluxes are formed with Roe's upwind-biased flux-difference splitting; the viscous terms are discretized by central differences.

The computational grid and the analysis locations are shown in Fig. 5. The grid level used is fine and the boundary conditions are Giles-type non-reflecting boundary conditions at the inlet and outlet of the domain. Essentially, the same grid is used for both the high Re and low Re CFD simulations. Firstly the grid for the high Reynolds number condition, that is, for the full scale stage configuration was constructed to have y+ close to 1.0 for all calculations. After that, the grid is automatically scaled down to be the target of low Reynolds number condition. Therefore the y+ for the low Reynolds number condition should be smaller, due to the thicker inlet boundary layer.

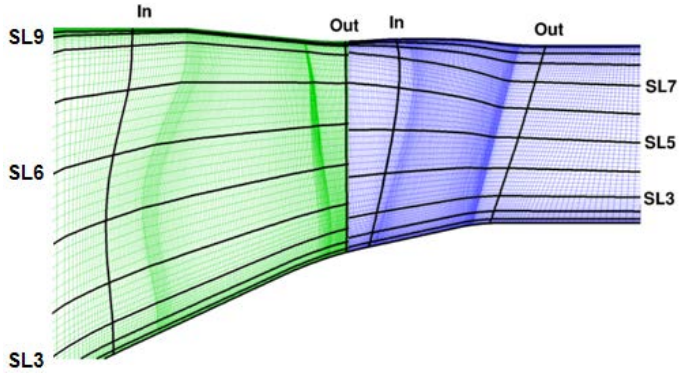


Figure 5. Computational grid and analysis locations.

RESULTS AND DISCUSSION

Assessment of CFD Code

In order to estimate the reliability of the TRACE code used in this research, a comparison of the fan stage performance map at low Re. number was made. Figure 6 shows this comparison of fan stage total pressure ratio (left) and the stage efficiency (right). The horizontal axis of the mass flow rate, the vertical axes of both the stage total pressure ratio (left) and the stage efficiency (right) are normalized by experimental values of the mass flow rate, total pressure ratio, and efficiency, at the

Copyright © 2013 by ASME

peak efficiency point for CRS, respectively. As mentioned in the experimental method section, the tight tip clearances of 0.10mm and 0.13mm were used for CRS and T/O conditions, respectively. While in the optimization the looser tip clearance of about three times has been used. Comparing EXP with CFD results (see "red" solid line: TCL=0.1mm) there is a better qualitative agreement at CRS for both stage total pressure ratio and efficiency, as compared to the looser TCL (0.3mm).

Figure 7 shows the experimental and numerical comparison of circumferentially averaged span-wise physical quantities at the rotor exit for PE point, CRS, low Re number. A good agreement between the CFD and EXP is obtained around the mid-span region, but a larger disagreement is observed around hub and tip endwall regions. Also, the effect of tip clearance is mainly observed from tip to mid-span (see rotor total pressure ratio: top left, total temperature ratio: top-right, and rotor exit flow angle: bottom-right).

In summary, there is a good qualitative agreement between EXP and CFD results. Thus, we move to the next section entitled "Effect of Reynolds Number on Performance".

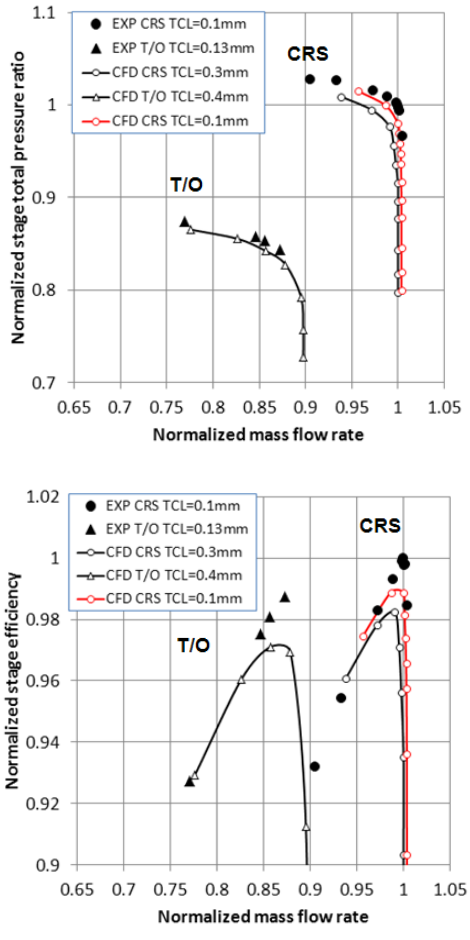


Figure 6. Experimental and numerical comparisons of fan stage performance at low Re number condition.

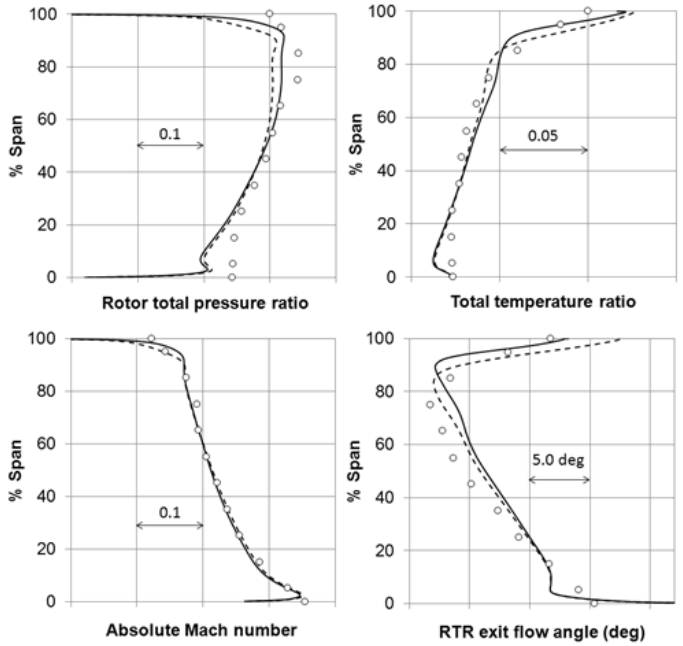


Figure 7. Experimental and numerical comparisons of span-wise physical quantity at rotor exit, PE, CRS, low Re number; circle: estimated value from EXP, solid line: CFD for TCL=0.1mm, dotted line: CFD for TCL=0.3mm.

Effect of Reynolds Number on Rotor Performance

Figure 8 shows the baseline rotor performance map for high and low Reynolds numbers. Both the total pressure ratio and the efficiency are decreased by the lower Reynolds number, by about 1% efficiency for both CRS and T/O conditions.

Figure 9 shows the spanwise distribution of physical quantities at the T/O PE condition for high (solid line) and low (dotted line) Reynolds number conditions. The Reynolds effect is observed across all span heights. In particular, total pressure ratio (top-left) is significantly reduced close to the hub for the low Reynolds number. This seems to be due to boundary layer separation as the Reynolds number at the hub section is the lowest (order of 10^5), as mentioned in the "Experimental Method". On the other hand, total temperature ratio is increased in the tip region at the low Reynolds number. Therefore the rotor efficiency is worse across all span-heights. Additionally the rotor loss coefficient is slightly worse for all span-heights, but the maximum deterioration is around the hub region at low Reynolds number.

Figure 10 shows the rotor blade surface Mach number distribution at around mid-span (SL5) and tip (SL9) at T/O PE condition for high (solid line) and low (dotted line) Reynolds number conditions. These span-wise positions relative to the blades are shown in Fig. 5. At the mid-span, the fluctuating Mach number distribution observed on both the suction-side and the pressure-side at a high Reynolds number is significantly suppressed at low Reynolds number. This may be

Copyright © 2013 by ASME

due to the reduced mass flow rate (see Fig. 8) and/or viscous behavior (thicker boundary layer thickness). Close to the tip, the shock system observed at 30% chord on the pressure-side is significantly reduced and shifted upstream at the low Reynolds number condition. The shock system observed around 50% chord on the suction-side is also shifted upstream, but the strength doesn't seem to change significantly.

In summary, the influence of Reynolds number on our rotor's efficiency is about 1%. The influence is observed along all span-height, especially the shock systems seen on both the suction-side and the pressure-side close to the tip, which are significantly changed.

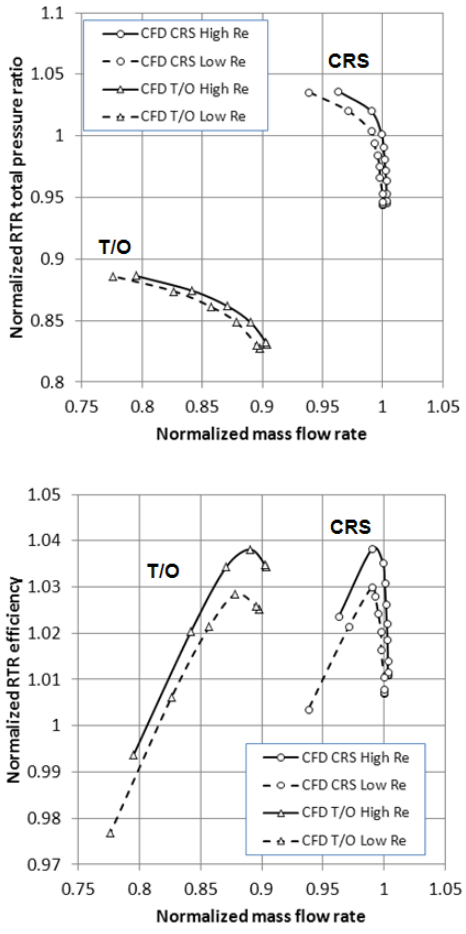


Figure 8. Comparison of rotor performance map between high and low Reynolds number conditions, top: normalized rotor total pressure ratio, bottom: normalized rotor efficiency.

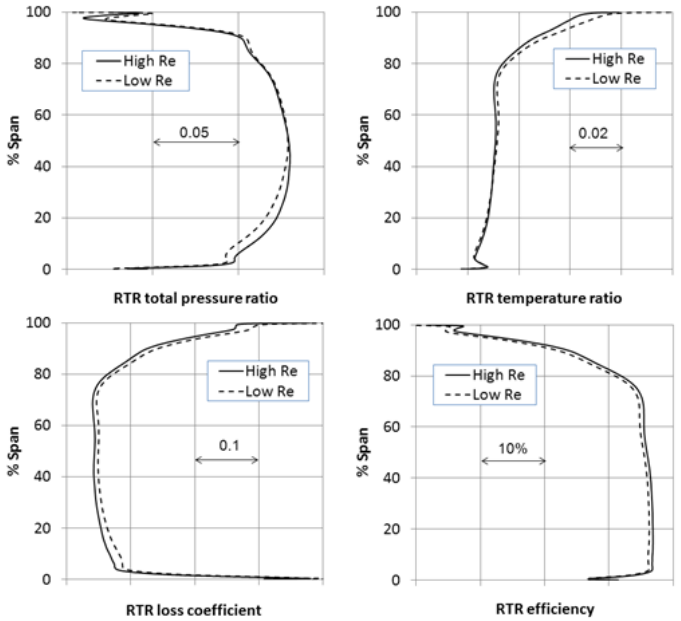


Figure 9. Comparison of span-wise physical quantity distribution at PE, T/O condition for high and low Reynolds numbers; solid line: High Re, dotted line: Low Re.

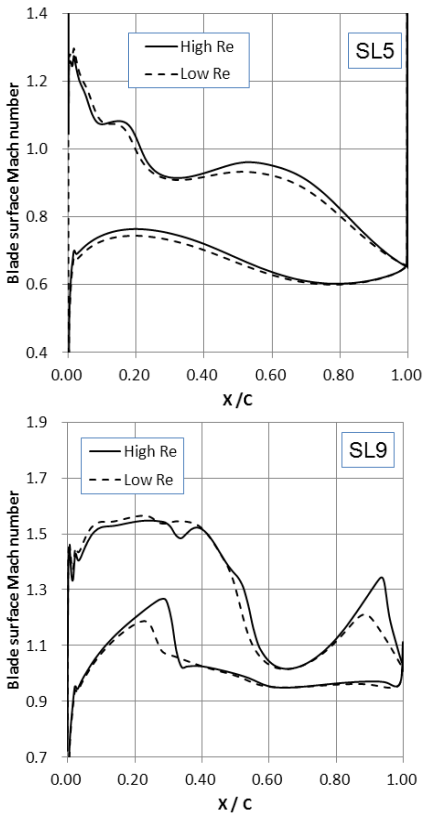


Figure 10. Comparison of blade surface Mach number distribution at around mid-span (top) and tip (bottom) at PE, T/O condition for high and low Reynolds numbers; solid line: High Re, dotted line: Low Re.

Copyright © 2013 by ASME

Re-Designed Fan Rotor Performance

The performance of the re-designed (optimized) rotor is shown in Fig. 11. On the left is the normalized rotor total pressure ratio and on the right is the normalized rotor efficiency, together with the baseline rotor. In general the performance characteristics are very similar to Fig. 3, obtained from Honda's isolated rotor simulations, although the increment of rotor efficiency (0.56%) obtained from the TRACE stage analysis is slightly smaller than that (0.88%) obtained from the Honda isolated rotor analysis.

In order to determine the similarity in the efficiency improvements between DLR and Honda simulations, the flow field for both baseline and optimized rotors were investigated. Figure 12-left shows a comparison of blade surface Mach number distribution at typical spanwise sections for the baseline and optimized rotors at PE, CRS condition. The left-top, left-middle, and left bottom show the hub-side (SL3), mid-span (SL6), and tip-side (SL9), respectively (also see Fig. 5). On the hub side (SL3), the Mach number distribution on the suction-side for the optimized rotor is relatively smooth and the decelaration of speed is quite reasonable, compared to the baseline, while the blade to blade loading at the leading-edge is significantly reduced. In the case of the mid-span (SL6), the Mach number distribution on the suction-side for the optimized rotor is once again relatively smooth and it seems that the shock system around 70% chord is weakened. Additionally the Mach number distribution along the pressure-side is quite reasonable and it seems that the shock system around 30% chord observed in the baseline is significantly improved. Near the tip (SL9) it seems that the shock system around 70% chord on the suction-side is also weakened and slightly shifted downstream. The shock strength observed on the pressure-side for the baseline is significantly reduced. It seems that this is due to the effect of negative curvature, as shown in Figs. 13 and 14. Also the blade to blade loading around the leading-edge is remakably reduced, a common chracteristic for all span-heights.

Figure 12-center and right show the comparison of Mach number contours at the same span-heights as the left figure. The same characteristics mentioned above are observed more clearly. Other characteristics are, as follows. At the mid-span, the leading-edge shock is detached for both the baseline and optimized rotors, while, at the tip, the shock is almost attached for both rotors. Here, in the case of the baseline a relatively larger low speed region behind an intersection of the passage shock from leading-edge-pressure-side with a leakage flow (vortex) is observed. However in the case of the optimized rotor such a strong low speed region is not observed. This may be the result of a weakened passage shock for the optimized rotor (see left-botom in Fig. 12).

The most remakable characteristic on the optimized rotor geometry is that a concave surface exists around the leading-edge (from 10% to 20% chord) on the pressure-side around the tip. As shown in Fig. 13, in the case of the baseline rotor, the suction-side curvature is almost "zero" like a plate, while the pressure-side curvature is positive (convex) on the frontal part of the airfoil. On the other hand, in the case of the optimized rotor, the suction-side curvature is positive until 20% chord, after that, negative (20% to 60% chord), and then positive again (60% to 100% chord). With respect to the pressure-side curvature for the optimized rotor, there is a region of negative curvature around 10% to 20% chord, as already mentioned above, after that, positive curvature (20% to 65% chord), then negative curvature again(65% to 100% chord). The geometry image of the airfoil's frontal part (0% to 40% chord) is shown in Fig. 14 where an exaggerated y-axis is used in order to give a better understanding of the differences in airfoil curvature between the baseline and optimized.

Based on the Honda in-house code [12], the negative curvature on the pressure-side around the leading-edge part plays an important role for the rotor efficiency. That is, there is a tendency of "the stronger the negative curvature is, the higher rotor efficiency is". However this is only valid at the design point. At part load, for example, at the T/O condition, stronger negative curvature leads to decreased efficiency. As mentioned in the introduction to this paper, cruise performance was our main objective and optimized directly, while the take-off and max climb performance were merely constrained to be equal to or better than the baseline. Therefore the degree of negative curvature is not so large.

In order to confirm the negative curvature effect, the pressure-side geometry around tip region for the baseline rotor was replaced with the same one for the optimized rotor. The peak efficiency at CRS was increased about 0.4%, about a half of the total efficiency increment of 0.88% suggested by the isolated CFD calculation in Honda [11].

In summary, the optimized rotor has superior efficiency to the baseline and one of the more interesting features is the negative curvature region from 10% to 20% chord on the pressure-side close to the tip.

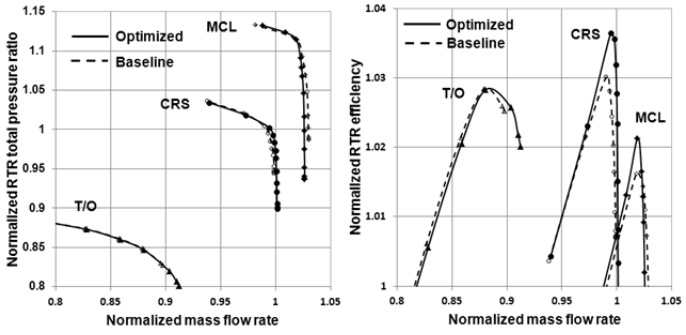


Figure 11. Comparison of rotor performance map between baseline and optimized at low Reynolds number conditions; left: normalized rotor total pressure ratio, right: normalized rotor efficiency.

Copyright © 2013 by ASME

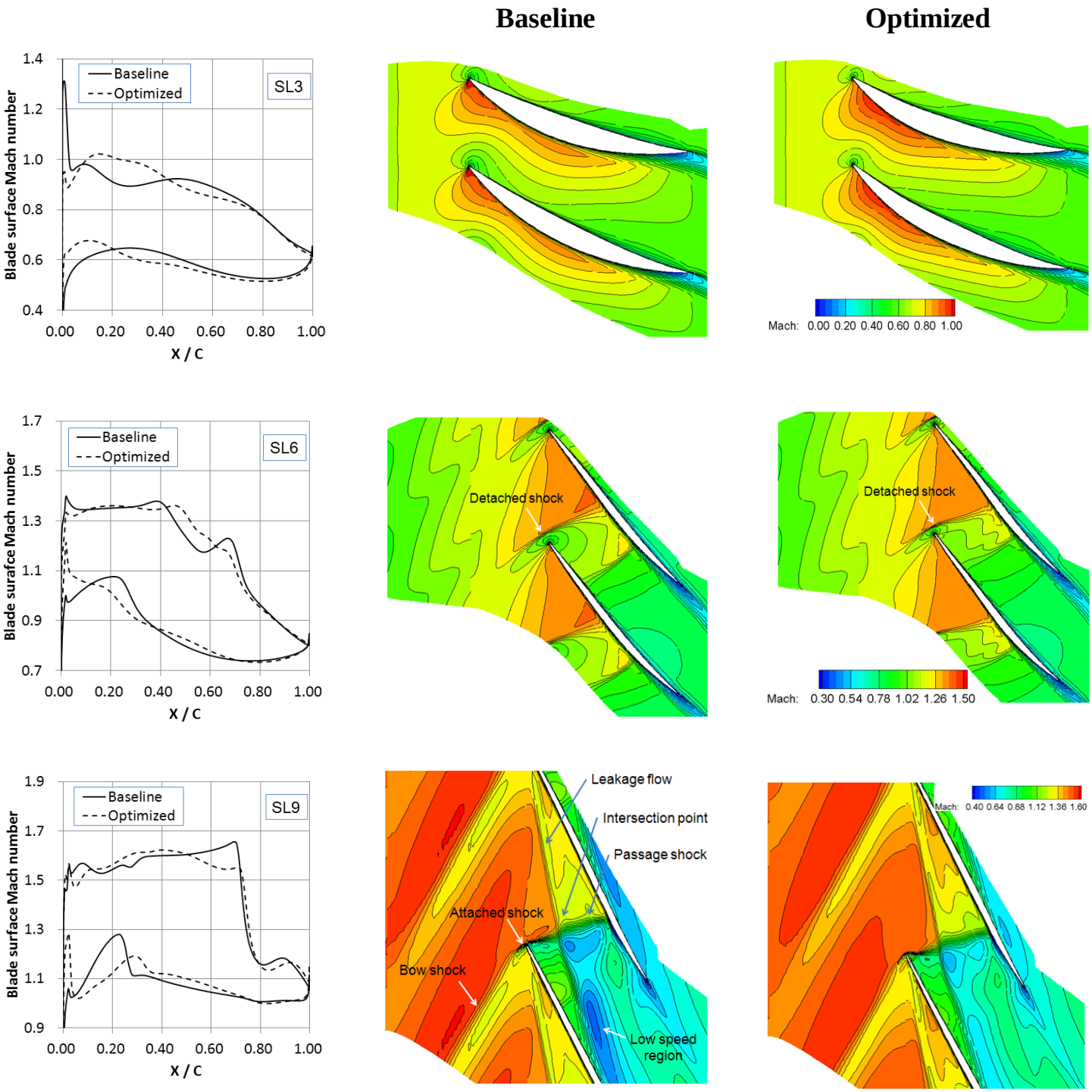
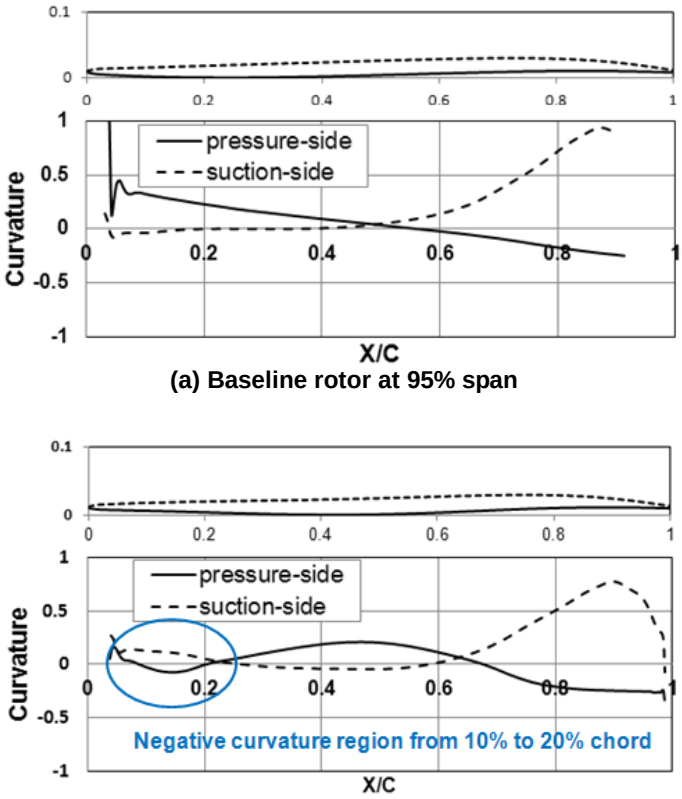


Figure 12. Comparison of rotor blade surafce Mach number (left; solid line: baseline, dotted line: optimized) and Mach number contours for baseline (middle) and optimized (right) at PE, CRS. Each span-height is shown by SL3, SL6, and SL9 and also see Figure 5.

Copyright © 2013 by ASME



(a) Baseline rotor at 95% span

(b) Optimized rotor at 95% span

Figure 13. Comparison of airfoil geometry at 95% span-height for Baseline and Optimized, (a) Baseline, (b) Optimized.

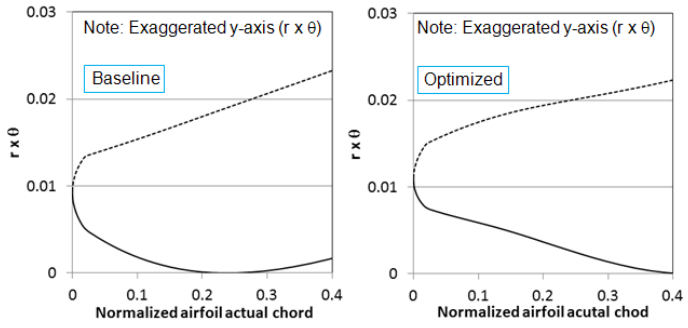


Figure 14. Detail airfoil geometry aroud frontal part (0% to 40% actual chord) at 95% span-height (left: Baseline, right: Optimized); Note: Exaggerated y-axis is used.

CONCLUSIONS

In this paper, Reynolds effects and the charecteristics of a re-designed transonic low-aspect ratio fan rotor working within a small turbofan engine have been investigated. The following conclusions can be drawn.

- There is a good qualitative agreement between EXP and CFD results for both performance map and span-wise physical quantity distribution.

- There are clearly Reynolds effects where the rotor efficiency is significantly decreased as the Reynolds number is decreased. The deterioration in efficiency is of the order of 1%.

- The redesigned rotor shows superior performance compared to the baseline rotor. The blade surface Mach number distribution along the airfoil chord at each span-height is significantly improved to provide both gradual flow deceleration and a weakened shock system.

- A unique airfoil geometry where there is a negative curvature region around airfoil frontal part on the pressure-side is observed on the optimized rotor. This is one of reasons why the optimized rotor has superior performance than the baseline.

REFERENCES

[1] Wassell, A. B., 1968, "Reynolds Number Effects in Axial Compressor," *Journal of Engineering for Power*, pp.149-156.

[2] Sonoda, T., Yamaguti, Y., Arima, T., Olhofer, M., Sendhoff, B., Schreiber, H. A., 2004, "Advanced High Turning Compressor Airfoils for Low Reynolds Number Condition, Part 1: Design and Optimization", ASME *Journal of Turbomachinery*, Vol. 126, No. 3, pp.350-359

[3] Schreiber, H.A., Steinert, W., Sonoda, T., and Arima, T., 2004, "Advanced High Turning Compressor Airfoils for Low Reynolds Number Condition, Part 2: Experimental and Numerical Analysis," ASME *Journal of Turbomachinery*, Vol. 126, No. 4, pp. 482-492.

[4] Sonoda, T., and Schreiber, H.A., 2007 "Aerodynamic Characteristics of Supercritical Outlet Guide Vanes at Low Reynolds Number Conditions", ASME *Journal of Turbomachinery*, Vol. 129, No. 4, pp. 694-704.

[5] Endicott, G., Sonoda, T., Olhofer, M., and Arima, T., 2011, "Aerodynamic Improvement of A Transonic Fan Outlet Guide Vane Using 3D Design Optimization," 2011, ASME Paper GT2011-46363.

[6] Sonoda, T., Arima, T., Endicott, G., and Olhofer, M., 2011, "A New Aerodynamic Design Concept for Transonic Swept Fan Outlet Guide Vanes," ISABE-2011-1224.

[7] Roeber, T., Kozulovic, D., Kuegeler, E., and Nuernberger, D., 2006, "Appropriate Turbulence Modeling for Turbomachinery Flows using a Two-Equation Turbulence Model," published in: New Results in Numerical and Experimental Fluid Mechanics V, Eds. Rath, H.J. et al., Springer, 2006.

[8] Franke, M., Röber, T., Kuegeler, E., and Ashcroft, G., 2010, "Turbulence Treatment in Steady and Unsteady

Copyright © 2013 by ASME

Turbomachinery Flows", Proceedings of the 5th European Conference on Computational Fluid Dynamics ECCOMAS CFD, June 2010.

[9] Nuernberger, D., Schmitt, S., and Eulitz, F., 2001, "Time Accurate Simulation of Turbomachinery Flow using an Implicit Time Integration Scheme," 39th AIAA Aerospcae Sciences Meeting and Exhibit, Reno, USA, AIAA 2001-0082.

[10] Schnell, R., Giebmanns, A., Nicke, E., and Dabrock, T., 2009, "Aerodynamic Analysis of a Fan for Future Ultra-High-Bypass-Ratio Aero Engines," ISABE Paper 2009-1149, ISABE Conference on Air Breathing Engines, Montreal/Canada.

[11] Endicott, G., Olhofer, M., Arima. T., and Sonoda, T., 2012, "Fan Rotor Multiple Conditions Optimization," Honda internal report.

[12] Arima, T., Sonoda, T., Shirotori, M., Tamura, A., and Kikuchi, K., 1999, "A Numerical Investigation of Transonic Axial Compressor Rotor Flow Using a Low-Reynolds-Number k-ε Turbulence Model," ASME *Journal of Turbomachinery*, Vol. 121, pp.44-58.

[13] Sederberg Thomas W. and Parry Scott R., 1986, "Free-form deformation of solid geometric models," SIGGRAPH Comput. Graph. 20(4):151{160, 1986. ISSN 0097-8930.

[14] Kennedy, J., and Eberhart, R., 1995, "Particle Swarm Optimization," Proceedings of IEEE International Conference on Neural Networks. **IV**. pp. 1942–1948. doi:10.1109/ICNN.1995.488968.

[15] Wennerstrom, A.J., 1984, "Experimental Study of a High-Throughflow Transonic Axial Compressor Stage," ASME *Journal of Engineering for gas turbines and Power,* Vol. 106, pp. 552-560.

Copyright © 2013 by ASME